ORIGINAL PAPER

Microseismic Monitoring to Characterize Structure-Type Rockbursts: A Case Study of a TBM-Excavated Tunnel

Quan-Sheng Liu[1,2] · Jian Wu[1,2] · Xiao-Ping Zhang[1,2] · Lie-Xian Tang[3] · Chen Bi[4] · Wei-Wei Li[4] · Jin-Lin Xu[4]

Abstract

Numerous rockbursts controlled by small-scale structural planes have occurred frequently during tunnel boring machine (TBM) excavation in a headrace tunnel. To understand the evolutionary process of structure-type rockbursts, a real-time microseismic (MS) monitoring system was deployed during the advancement of TBM. By combination with the true reflection tomography technique, a new method is proposed to estimate the P-wave velocity for in situ hypocentral locations. A typical structure-type rockburst is investigated to study the relationship between the rockburst characteristics and microseismicity. By further analyzing the temporal–spatial distribution of microseismicity and the quantitative interpretation of the MS source parameters, the potential failure zone and the precursor features are recognized during the development of this structure-type rockburst. Based on the MS monitoring results, some proactive treatment measures are put forward for the mitigation of rockburst hazards. The results of the current research can contribute to the understanding of structure-type rockbursts and provide valuable references for rockburst forewarning and construction management in similar tunneling projects.

List of Symbols

σ_m	Maximum principal stress
k	Number of monitoring cross-sections
$t_{k+1,\mathrm{p}}$, $t_{k,\mathrm{p}}$	Arrival time of P-wave at $(k+1)$-th and k-th monitoring cross-section
Δt	Arrival time differences of P-wave between monitoring cross-sections
ΔL	Distance between the $(k+1)$-th and k-th monitoring cross-sections
v_p	Velocity of P-wave
D	Relative magnitude of P-wave velocity
v_max	Maximum relative P-wave velocity
v_min	Maximum relative P-wave velocity
v_e	Equivalent velocity of P-wave
L	Distance from MS source to sensors
t	Propagation time from MS source to sensors
L_i	Length of the i-th section
$v_{\mathrm{p}i}$	P-wave velocity at the i-th section
E	Seismic energy
E_p	Seismic energy of P-wave
E_s	Seismic energy of S-wave
M	Seismic moment
ρ	Rock mass density
v	Velocity of body wave (P-wave or S-wave)
R	Hypocentral distance from MS source to sensors
J_c	Energy flux
F_c	Average radiation coefficient
Ω_oc	Spectral level of P-wave or the vector sum of the components of S-wave
σ_A	Apparent stress
V_A	Apparent volume
K	Stiffness of rock mass
EI	Energy index
M_0	Measured seismic moment
$\bar{E}(M_0)$	Mean radiated energy
d, c	Fitting constants

✉ Xiao-Ping Zhang
jxhkzhang@163.com

1 Key Laboratory of Safety for Geotechnical and Structural Engineering of Hubei Province, School of Civil Engineering, Wuhan University, Wuhan 430072, China

2 Key Laboratory of Rock Mechanics in Hydraulic Structural Engineering of the Ministry of Education, Wuhan University, Wuhan 430072, China

3 School of Mining Engineering, University of Science and Technology Liaoning, Anshan 114051, China

4 Sinohydro Bureau 3 Co., Ltd., Xi'an 710000, China

Abbreviations

CGIHE	Code for geologic investigation of hydropower engineering
DAC	Digital-to-analogue converter
DB	Drill-and-blast
ESG	Engineering seismology group
FFT	Fast Fourier transform
HNAS	Hyperion network acquisition system
MS	Microseismic monitoring
STA/LTA	Short time average vs. long time average
TBM	Tunnel boring machine
TRT	True reflection tomography
UCS	Uniaxial compressive strength
WT	Wavelet transform

1 Introduction

Rockburst is a type of common and violent excavation-induced disaster that occurs within overstressed rock mass, posing a great threat to the safety of workers and the efficient construction of underground projects (Cook 1965; Hoek and Brown 1980; Zhang et al. 2012a, b; Feng et al. 2013). Under conditions of high in situ geo-stress, the heterogeneity of rock masses and complex geological structures are closely related to the occurrence of rockbursts due to stress concentration (Mazaira and Konicek 2015; Naji et al. 2019). As excavations become deeper, more cases of rockbursts have been reported (Kaiser et al. 1996; Feng et al. 2012; Lu et al. 2018), which are significantly associated with special geological structures, such as regional faults, discontinuities and composite folds (Trifu and Shumila 2010; Feng et al. 2013; Zhao et al. 2017). For instance, many researchers have found that the occurrences of intensive rockbursts and large-magnitude tremors were closely related to reactivated faults in underground projects (Mcgarr et al. 1989; Zhang et al. 2012a; Feng et al. 2013). Ortlepp (2000) provided a detailed exploration for the extremely violent fracturing phenomena induced by fault structures in a deep South African gold mine. Zhang et al. (2014) explored the fracture process of a rock mass induced by an activated fault for hundreds of meters of the Shirengou iron mine. Michael and Thomas (2018) found that the presence of a major tectonic fault had adverse effects on the stress concentration within the region of rockbursts. The relationship between geologic discontinuity and induced seismicity has also been widely explored (Snelling et al. 2013; Xiao et al. 2016a). Tang et al. (2010) investigated the effects of structural planes on inducing rockbursts in the Jingping II Hydropower Station. Wang et al. (2018) found that axis of syncline structures with high-stress regions presented larger rockburst hazards in coalmines.

These previous studies were mainly focused on the unfavorable effects of large-scale geological abnormity bodies (e.g., regional faults and syncline regions) on rockbursts. These bodies may be reactivated by extensive excavation disturbances in mines and underground caverns (Ortlepp 2000; Li et al. 2017b). The disturbance level often depends on the excavation parameters, such as the excavation geometry, advance rate, mining extraction ratio and excavation methods (i.e., tunnel boring machine (TBM) and drill-and-blast (DB) methods) (Ortlepp 2000; Zhang et al. 2012b). However, the excavation dimensions of civil tunnel projects are usually only several meters. The excavation areas of these tunnels are much smaller than those of mines and underground caverns, as is the stress disturbance of the surrounding rock mass (Mazaira and Konicek 2015). Large-scale geological abnormity bodies cannot be easily reactivated during tunnel excavation (Zhou et al. 2014; Ma et al. 2018). In a headrace tunnel of the present study, the majority of the small-scale structural planes of approximately 10–20 m intersected with the axis of this tunnel according to the in situ geological investigation. The locations of most rockbursts were primarily consistent with the intersecting areas of these structural planes. Occurrences of rockbursts are largely determined by the stress states of rock masses and the characteristics of small-scale structural planes. To date, few studies have been conducted to explore the relationship between in situ rockburst characteristics and small-scale structural planes in TBM-excavated tunnels. The evolutionary process and fracturing mechanism of rockbursts associated with small-scale structural planes have not been fully understood.

Microseismic (MS) monitoring techniques have already become an effective and applicable tool to capture the evolutionary process of rockbursts in underground engineering, such as in deeply buried tunnels (Ma et al. 2015; Xu et al. 2016; Liu et al. 2018), underground caverns and mines (Mendecki 1997; Leśniak and Isakow 2009; Hudyma and Potvin 2010). By capturing the time of occurrence, location and intensity of MS events, potential rockburst areas with active microseismicity can be identified (Dai et al. 2016a; Xiao et al. 2016a). Moreover, the fracturing processes of rock masses, namely the initiation, propagation and coalescence of micro- and macro-fractures, can be recognized through the interpretation of recorded MS information (Young et al. 2004; Glazer 2016). Based on MS information, the dynamic fracturing characteristics of rock masses can be acquired during the development of structure-type rockbursts. Then, the evolutionary process of structure-type rockbursts can be obtained through the MS monitoring technique. Further research can be presented in the interpretation

and forewarning of rockbursts controlled by small-scale structural planes.

In the present study, to understand the evolutionary process of rockbursts associated with small-scale structural planes, a real-time and moveable MS monitoring system was deployed in a TBM-excavated headrace tunnel in China. The characteristics of a typical structure-type rockburst are analyzed in detail. Efforts are made to reveal the relationship between rockburst characteristics and the induced microseismicity. The MS information concerning the effects of structural planes is quantitatively analyzed to explore the evolutionary process of rockbursts. Therefore, the potential failure zones and the MS precursor features of rockbursts associated with small-scale structural planes are revealed. Some proactive treatment measures are suggested for the mitigation of rockburst hazards based on the MS monitoring results.

Table 1 Main specifications of TBM1

Technical parameters	Design value
TBM type	Open
TBM diameter (m)	6.53
TBM length (m)	210
TBM weight (tons)	Approx. 1240
Cutterhead nominal torque (kN m)	4510
Cutterhead maximum thrust (kN)	23,267
Cutterhead power (kW)	$350 \times 8 = 2800$
Rotational speed (rpm)	0–9.8
Thrust cylinder stroke (mm)	1900
Conveyor capacity (t/h)	1000

2 Fracturing Characteristics of In Situ Structure-Type Rockbursts

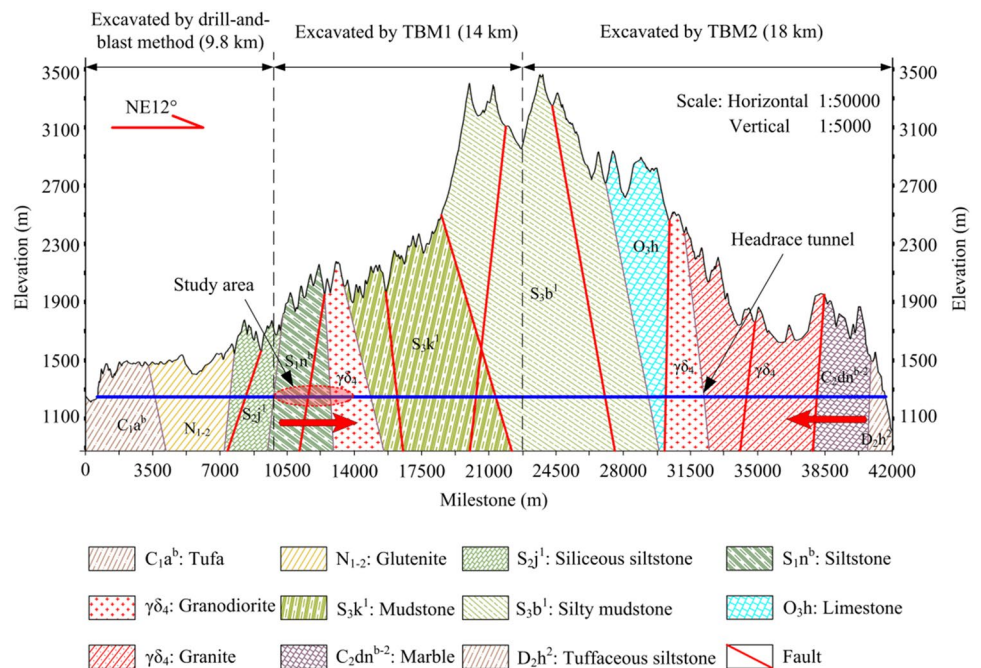### 2.1 Project Description and Geological Condition

The headrace tunnel project is located in Northwestern China. This tunnel has an excavation length of 41.8 km and a maximum buried depth of 2268 m. About 32 km of the tunnel section will be excavated by two TBMs. The remaining section will be constructed by the DB method. The main specifications of TBM1 of the present study are listed in Table 1. The corresponding geological profile along the headrace tunnel is presented in Fig. 1.

This project region is characterized by Variscan orogeny, where the principal strata belong to the Silurian and Middle Variscan period. The main rock type along this tunnel consists of siliceous siltstone of the Nileke group (S_1n), medium–thick metasiltstone of the Jifuke group (S_2j), metamorphic mudstone and fine sandstone of the Kuruer group (S_3k) and Variscan granodiorite ($\gamma\delta_4$). According to the geological investigation of the outcrop and the tectonic history of the project area, the tunnel traverses the Borokonu complex anticline, which strikes nearly east to west with a moderate or steep dip. The strong squeeze folds, secondary folds and faults in these rock formations are well developed, which may have an important influence on the distribution of the geo-stress field. There are mainly four groups of steep faults, which are in the EW direction, NNW direction, NW direction and NE direction. The uniaxial compressive strength (UCS) of the rock in the study

Fig. 1 Geological profile along the headrace tunnel

area (Fig. 1) is approximately 80–130 MPa, and its elastic modulus and Poisson ratio are approximately 40–60 GPa and 0.1–0.3, respectively. The surrounding rock mass of this headrace tunnel is mainly classified as Class III and Class IV, accounting for 53 and 29%, respectively. This classification method is based on the Code for Geologic Investigation of Hydropower Engineering (CGIHE), which is proposed by the National Standards Compilation Group of the People's Republic of China (GB50487-2008) (2008).

Due to the regional tectonic movement and the deep-buried depth, high geo-stress is expected within the surrounding rock mass of this tunnel. The overcoring method was carried out to measure the geo-stress (Wohnlich 1999; Sjöberg et al. 2003; Krietsch et al. 2018). This method shows that the maximum principle stress (σ_m) at milestone K13 + 169 m (buried depth of 740 m) is approximately 33.4 MPa, and the direction of the maximum principal stress is nearly horizontal. The second principal stress and the minimum principal stress are approximately 25.3 MPa and 22.6 MPa, respectively. At a depth of more than 2000 m, it can be roughly estimated that the maximum principal stress (σ_m) can surpass 60 MPa, according to the buried depth.

2.2 Statistics of Rockbursts in TBM Tunnels

From 1 February 2018 to 1 September 2018, 152 rockbursts occurred in the headrace tunnel between milestones K9 + 500 and K14 + 300 (buried depth of 450–950 m). Due to the simplicity and flexibility of the CGIHE method, it is commonly adopted to evaluate rockburst intensities in the water conservancy and hydropower industry in China (Feng et al. 2013; Liu et al. 2016, 2017). Based on the phenomena of in situ rockbursts, the intensity classifications of rockbursts in the CGIHE method are shown in Table 2 (Chen et al. 2015). The distribution of rockbursts with different intensities is shown in Fig. 2. Mild and moderate rockbursts
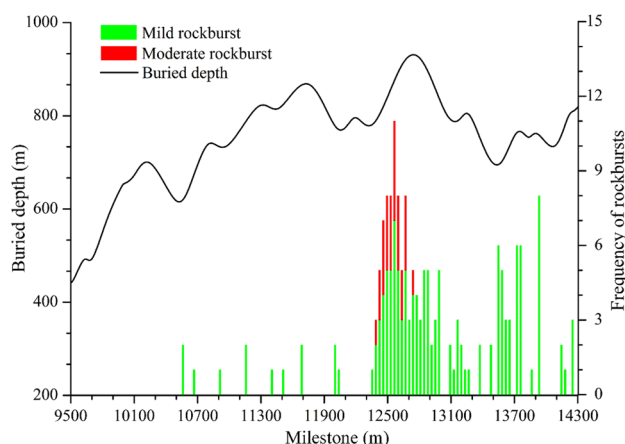

Fig. 2 Distribution of rockbursts between milestones K9 + 500 and K14 + 300 m

account for 79.2% and 20.8%, respectively. The frequency of rockbursts increases significantly with the increase in the buried depth. Therefore, moderate-to-intense rockbursts are expected to occur during the excavation of the headrace tunnel at buried depths from 950 to 2000 m.

The relationship between the frequency of rockbursts and the distance to the tunnel face is presented in Fig. 3. Most of the observed rockbursts are located behind the tunnel face within 15 m. The frequency of rockbursts decreases significantly with increasing distance to the tunnel face. Moreover, most rockbursts are usually associated with structural planes, mainly occurring at the sidewalls and the crown of the tunnel. The rockburst notches have depths of 0.3–1.0 m and lengths of 0.6–7.0 m. The boundaries of rockburst notches are usually controlled by small-scale and rigid structural planes. Therefore, to explore the locational relationship between rockbursts and small-scale structural planes, the attitudes of small-scale structural planes were investigated at

Table 2 Rockburst intensity classifications in the CGIHE method (The National Standards Compilation Group of People's Republic of China 2008)

Rockburst levels	Phenomena (main failure type, sound and depth of notches)	Classification standard UCS/σ_m
Mild	Slight spalling and slabbing in the surface of the surrounding rock mass. Rock mass is not ejected. The depths of the notches are less than 0.5 m. Cracking sound can be heard occasionally. Construction is not affected	4–7
Moderate	Severe spalling and slabbing of the surrounding rock mass. Rock mass is slightly ejected. Cracking sounds like a detonator blasting inside the rock mass. The depths of the notches range from 0.5 to 1.0 m. Construction is barely affected	2–4
Intense	A large amount of rock mass is suddenly ejected. The failure sounds like an explosive blast. The depths of the notches range from 1.0 to 3.0 m, with an extensive failure range. Construction will be affected to some extent	1–2
Extremely intense	A large block of rock mass is suddenly ejected with intensive seismicity. The stability of the whole carve is seriously affected. The failure sounds like thunder or a cannonball. The depths of the notches are greater than 3.0 m, with a large rock fragment size. Construction is seriously affected	< 1
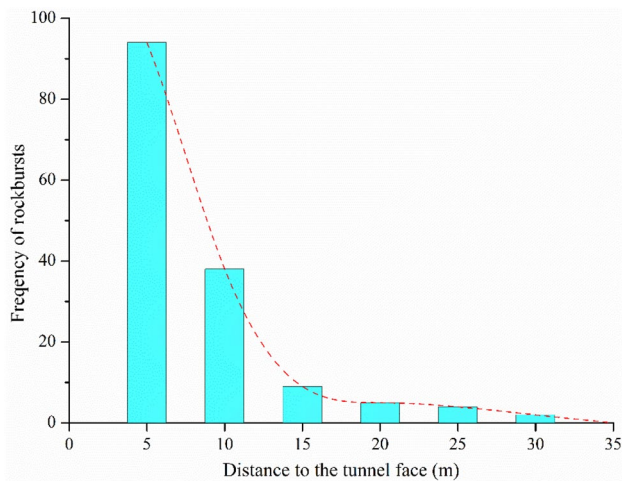
Fig. 3 Relationship between the frequency of rockbursts and the distance to the tunnel face
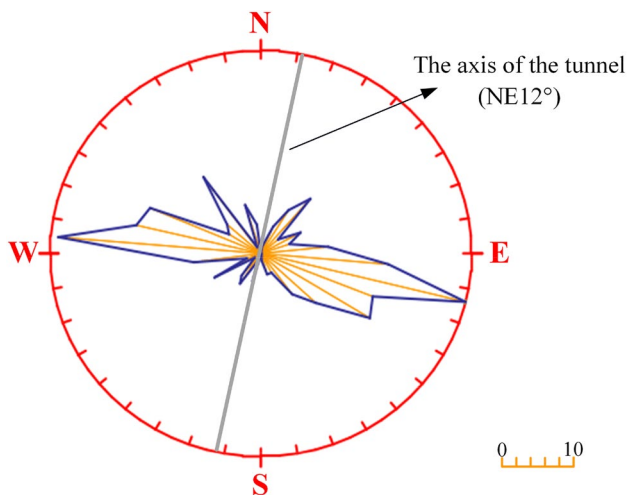
Fig. 4 Rose diagram of the dip directions of small-scale structural planes

the tunnel section (study area in Fig. 1). The rose diagram of the dip directions of small-scale structural planes is shown in Fig. 4. The dip direction of the dominating small-scale structural planes is approximately perpendicular to the tunnel axis. After excavation unloading, the presence of these structural planes contributes significantly to the formation of an adverse stress concentration at the periphery of the tunnel.

2.3 Characteristics of the 4.13 Rockburst

At approximately 21:55 on 13 April 2018, a typical rockburst controlled by small-scale structural planes occurred in the left sidewall from milestones K12 + 390 to K12 + 400 m (Fig. 5a), referred to as the '4.13 rockburst' below. The

buried depth of this rockburst region is approximately 780 m, which is comparable with the buried depth (740 m) of the geo-stress measurement location (K13 + 169 m). It can be inferred that the maximum principle stress at milestones K12 + 390–12 + 400 m is comparable to that at K13 + 169 m, where the measured value is 33.4 MPa. The lithology around this rockburst zone is siliceous siltstone formations with a UCS of approximately 105.0 MPa. The ratio of the rock mass strength to the in situ stress (UCS/σ_m) is calculated as approximately 3.2. The rockburst notch, with a maximum length and depth of 7.0 m and 0.6 m, respectively, has a V-shaped appearance in Fig. 5b. According to the in situ characteristics of the 4.13 rockburst, it can be classified as moderate rockburst based on the CGIHE method. Moreover, it is obvious that the boundary of the 4.13 rockburst is controlled by two intersected rigid structural planes with no filling. The attitudes of these two structural planes are NE55°∠78° and SE60°∠70°, respectively. Thus, the rock mass at the left sidewall is pre-cut by two intersected structural planes with an intersection angle of approximately 110°. Before the 4.13 rockburst, several mild rockbursts occurred from milestones K12 + 390 to K12 + 400 m, indicating the redistribution and adjustment of stress after excavation unloading. Micro-cracks may have gradually initiated when the stress concentration occurred at the localized area of the intersected structural planes. As the stress magnitude increased, the cracks propagated and coalesced along the pre-existing rigid structural planes. When the stored strain energy exceeded a critical level within the localized rock mass, the sudden release of the strain energy occurred. Part of the energy was dissipated through the fracturing of cracks, and the remaining energy was transformed into kinetic energy for the ejection of fragments. Then, the typical V-shaped notch formed towards the openings.

A volume of rock mass fragments has been ejected from the left sidewall (Fig. 6a). The fragments are characterized by angular and clastic shapes with different dimensions. The surfaces of the fragments are smooth and without scratches. These attributes are characteristic of brittle tensile failure. The H-shaped steel arches used for support in the vicinity of the notch are deformed and dislocated by collisions of rock mass fragments (Fig. 6b). Effective support measures, such as rock bolts and steel meshes, should be taken to resist the rockburst.

3 In Situ Microseismic Monitoring

Due to the fracturing of rock masses caused by stress concentrations, elastic strain energy is released in the form of seismic waves. The waves can be detected as MS signals by sensors. By the processing of the MS signals, the dynamic evolutionary laws of the source parameters can be obtained

Fig. 5 Photographs of the 4.13 rockburst. **a** Rockburst zone, **b** V-shaped notch, **c** rigid structural planes, **d** well-developed structural planes at milestones K12 + 390–12 + 400 m
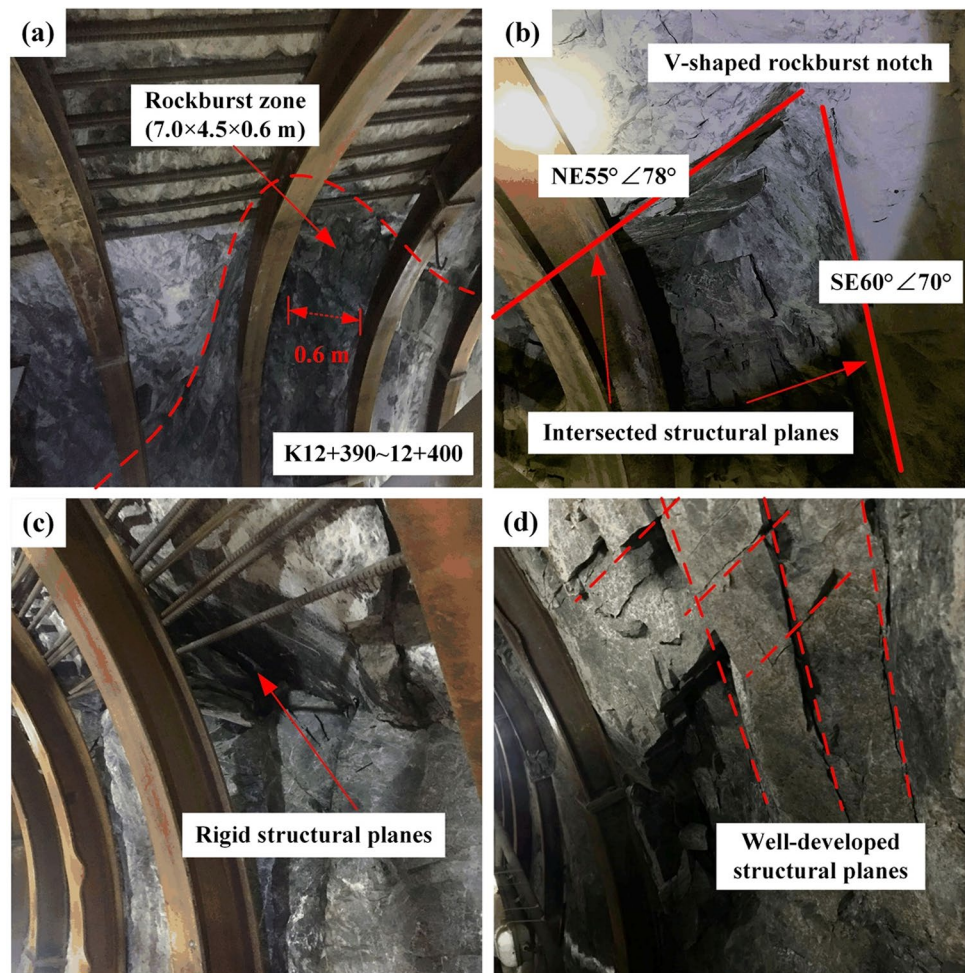
Fig. 6 **a** Rock mass fragments, **b** dislocation of steel arch in the 4.13 rockburst
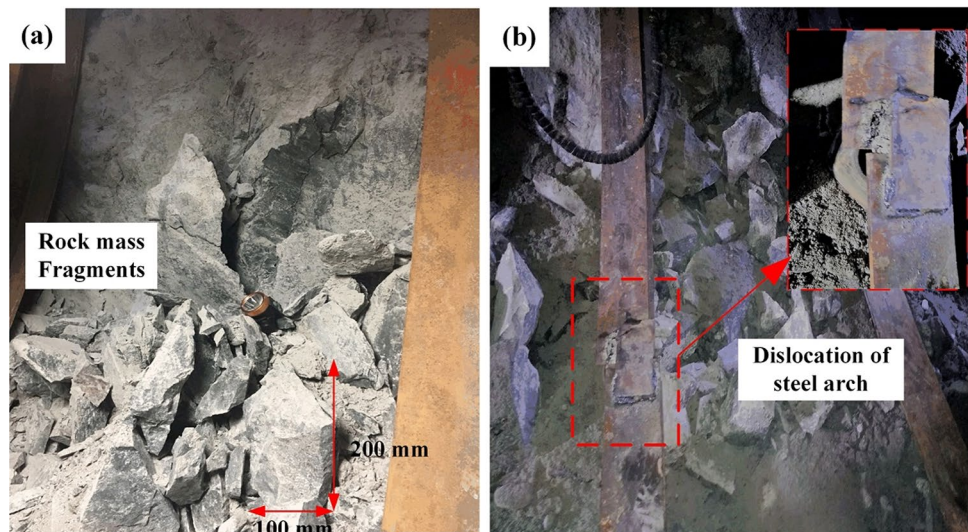
quantitatively, such as the location, radiated energy, seismic magnitude, apparent stress and apparent volume. These parameters are used to analyze the characteristics of microseismicity during the development of fracturing. These characteristics can reveal the potential fractured regions and failure precursors in the surrounding rock mass. Therefore, the MS monitoring technique can be used to provide early warning of rockbursts and to understand the evolutionary

process of fractures (Zhang and Zhang 2017; Zhang et al. 2017).

3.1 Configuration of the MS Monitoring Scheme

To deliver a continuous stream of real-time information about the fracturing behavior, a high-resolution MS monitoring system (Engineering Seismology Group (ESG), Canada) was used in the headrace tunnel of the present study. The MS monitoring system consists of a portable Paladin IV, six uniaxial accelerometers, cables and installation beams (Fig. 7). The portable Paladin IV is integrated with the powerful Hyperion seismic processing and digital signal acquisition system, possessing a 32-bit delta-sigma digital-to-analogue converter (DAC) and a sampling frequency of 10 kHz, respectively (Urbancic and Trifu 2000; Tang et al. 2010). The uniaxial accelerometers have a frequency response range of 50 Hz–5 kHz and a sensitivity of 30 V/g. The sensor array is located behind the tunnel face of 80 m to ensure personnel and equipment safety. Six uniaxial accelerometers are mounted in the borehole at a depth of approximately 1.5 m and are distributed at three cross-sections with an interval of 35 m. When the excavation distance reaches 35 m, the accelerometers of the last cross-section are recycled and moved forward to the front, constituting the first cross-section. The layout of the MS monitoring system is shown in Fig. 8.

When MS events are detected, the accelerometer can generate associated analogue waveform signals. The digital signal acquisition system of the portable Paladin IV converts the analogue waveform signals into digital signals with 32-bit resolution. Then, these digital signals can be recorded and processed by the ESG software programs: hyperion network acquisition system (HNAS) and waveform visualizer (WaveVis). The HNAS program is configured to automatically remove noise from waveform signals and identify the initial pulse of P-waves or S-waves using the short time average vs. long time average (STA/LTA) algorithm (Xu et al. 2011). The WaveVis program is visualization software that provides a method of graphically displaying seismic waveforms. Thus, the seismic event data can be processed and analyzed by the ESG system to obtain the locations of MS events and the source parameters, which can be stored in a variety of formats and accessed by other programs.
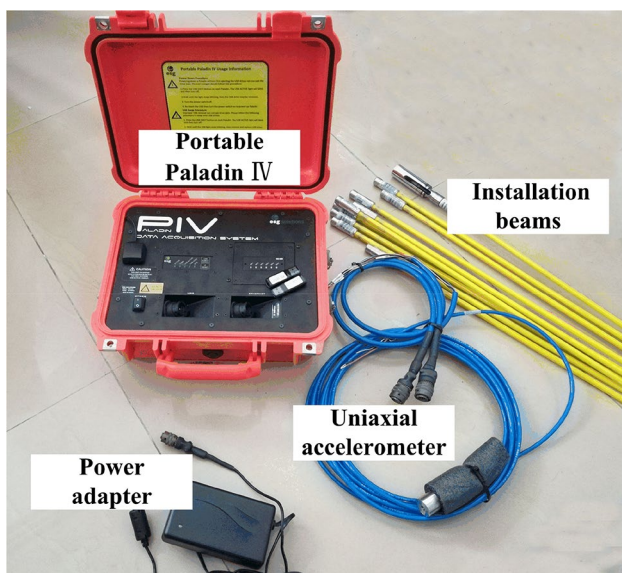
3.2 Recognition of MS Signals

The seismic signals recorded by MS monitoring system usually contain a number of noise signals, such as mechanical knock, TBM vibration and electrical noise. Therefore, the data of seismic signals should be refined to identify the useful MS signals concerning the fracturing of the rock mass. By acquiring in situ waveforms of different source types, the typical waveforms of noise signals and MS signals are presented in Fig. 9. The MS signals of fracturing have different time-domain features compared to those of the noise signals. Moreover, the waveform parameters in the frequency domain can be obtained by the fast Fourier transform (FFT) and wavelet transform

Fig. 7 Constitution of the MS monitoring system

Fig. 8 Vertical view of the layout of the MS monitoring system
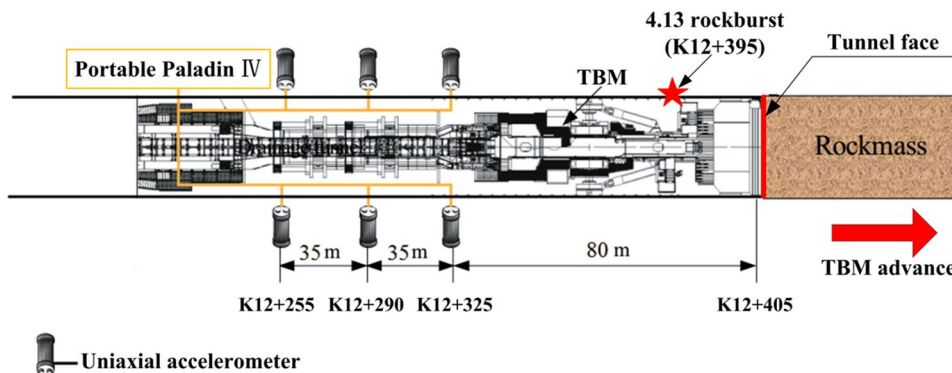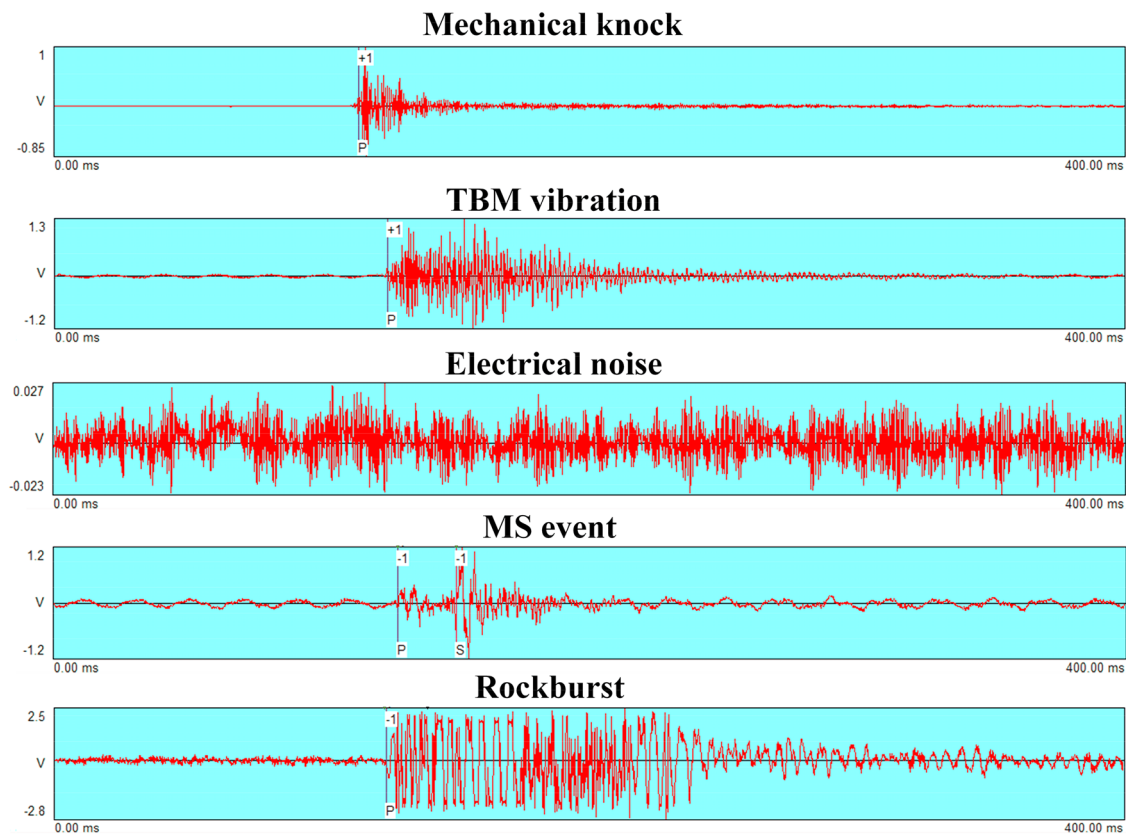
Fig. 9 Typical waveforms of various seismic signals

(WT) methods (Mallet 1999). Therefore, the characteristics of the seismic signals derived from the waveforms in the time domain and frequency domain can be summarized in Table 3. By extracting the main waveform features of different signals, the recognition of valid MS signals can be achieved.

3.3 Estimation of the P-Wave Velocity

The estimation of the P-wave velocity is critically important for the accurate location of MS signals. In previous studies, the fixed-point blasting method was widely used to determine the P-wave velocity of rock masses (Dai et al. 2016b; Zhao et al. 2017). However, due to the limitations of construction conditions and the safety considerations

Table 3 Main characteristics of different seismic signals

Typical signals	Main characteristics
Mechanical knock	The duration of the mechanical shock signal is generally less than 150 ms and is accompanied by an undeveloped coda wave. The arrival time of the S-wave is not obvious. The dominant frequency of a mechanical shock signal is apparent, with a range of 1500–2000 Hz
TBM vibration	The duration of a TBM vibration is approximately 200 ms. The coda wave is developed. It is difficult to pick the arrival time of the S-wave. The dominant frequency mainly ranges from 500 to 1000 Hz
Electrical noise	Electrical noise has a long duration and is usually mixed with other signals. The amplitude of the waveform is relatively small. The dominant frequency is mainly concentrated from 2000–2500 Hz
MS event	The duration of a MS event is approximately 70–150 ms. It is easy to pick the arrival times of the P-wave and S-wave. Low frequencies dominate, with a range of 130–300 Hz
Rockburst	A rockburst waveform has a duration approximately 200–300 ms, accompanied by well-developed coda waves and the phenomenon of peak dissipation. The amplitude of the waveform is relatively large. The arrival time of the S-wave is difficult to identify. The dominant frequency is obvious, ranging from 125 to 280 Hz

of in situ blasting, artificial blasting tests are impractical to carry out in TBM tunnels. Thus, in the present study, a new method is proposed to estimate the average P-wave velocity using the MS monitoring system combined with the true reflection tomography (TRT) technique.

At the present construction stage, the ahead geological prospecting technique TRT is conducted to evaluate the geological conditions ahead of the tunnel face within a range approximately 120 m. The physical basis of TRT is the relative differences between the physical properties of different rock masses, such as the P-wave velocity and density (Otto et al. 2002; Yamamoto et al. 2011). Using the controlled sources and sensors installed on the tunnel sidewalls, the technique of TRT can receive and process the reflected seismic signals caused by the impedance contrast due to the geological and lithological differences. Sufficient information on the spatial wave field can be obtained by TRT (Cheng et al. 2014; Li et al. 2017a). Then, the relative P-wave velocity of the rock mass can be obtained from the reflection of the seismic waves. Furthermore, when the MS signals are acquired by the sensors, the arrival time differences can be manually picked to calculate the average P-wave velocity between the sensor arrays using Eq. (1). Then, the P-wave velocity of the rock mass ahead of the tunnel face can be estimated based on the relative change and the calculated P-wave velocity:

$$v_{\mathrm{p}} = \frac{\Delta L}{\Delta t} = \frac{\Delta L}{t_{k+1,\mathrm{p}} - t_{k,\mathrm{p}}}, \tag{1}$$

where v_{p} is the velocity of the P-wave between the sensor arrays; ΔL is the distance between the $(k+1)$-th and k-th monitoring cross-sections; Δt is the differences in the arrival time of the P-wave between the monitoring cross-sections; and $t_{k+1,\mathrm{p}}$ and $t_{k,\mathrm{p}}$ are the arrival times of the P-wave at the $(k+1)$-th and k-th monitoring cross-sections, respectively ($k = 1, 2$). For instance, within the tunnel sections covered by sensor arrays at milestones K12 + 290–12 + 325 m, the average P-wave velocity of the surrounding rock mass is calculated as 5849 m/s using Eq. (1). According to the results of ahead geological prospecting at milestones K12 + 290–12 + 410 m, the variation of the relative P-wave velocity can be normalized using Eq. (2). Therefore, the P-wave velocity of the rock mass at milestones K12 + 290–12 + 410 m (Fig. 10) can be estimated according to the relative P-wave velocity:

$$D = \frac{v - v_{\min}}{v_{\max} - v_{\min}}, \tag{2}$$

where D is a dimensionless value ranging from 0 to 1 and represents the relative magnitude of the P-wave velocity; and $v_{\max}$ and $v_{\min}$ are the maximum and minimum relative
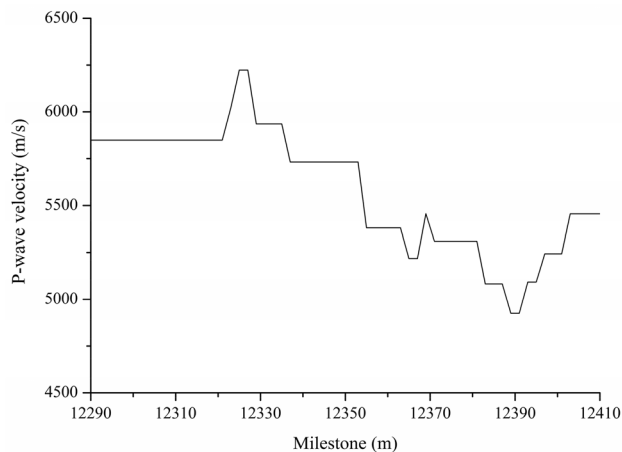

Fig. 10 P-wave velocity of the rock mass at milestones K12 + 290–12 + 410 m

P-wave velocities, respectively, which are measured by TRT at milestone K12 + 290–12 + 410 m.

In the ESG monitoring system, a simplified single-velocity model is adopted to locate MS events using the Geiger iteration algorithm, which has been widely used in many fields for hypocentral location (Feng et al. 2013). According to the P-wave velocity calculated above, an equivalent velocity of the P-wave is estimated for the MS source location in the single-velocity model using the following equation:

$$v_{\mathrm{e}} = \frac{L}{t}$$
$$t = \sum_{i=1}^{n} \left(\frac{L_i}{v_{\mathrm{p}i}} \right), \tag{3}$$

where v_{e} is the equivalent velocity of the P-wave; L is the distance from the MS source to the sensors; t is the propagation time from the MS source to the sensors; i is the number of sections with different P-wave velocities; L_i is the length of the i-th section; and $v_{\mathrm{p}i}$ is the P-wave velocity of the rock mass at the i-th section. Then, according to the P-wave velocity of the rock mass between the rockburst and the sensor at milestones K12 + 325–12 + 395 m in Fig. 10, the equivalent velocity of the P-wave can be calculated as 5545 m/s using Eq. (3).

For the 4.13 rockburst at the milestone K12 + 395 m, the location of the rockburst range can be measured directly. Meanwhile, the related MS event clusters associated with the main fracture are recognized in the ESG monitoring system. The location coordinates of the related MS events can be processed as shown in Table 4. However, it is difficult to obtain the actual locations of the related MS events in the range of the rockburst (Fig. 5a). Then, the geometric center of this V-shaped rockburst notch is assumed as the reference location for the related MS events (Fig. 11). The measured

Table 4 Location distance between the related MS events and the reference point

MS events no.	Coordinates of the related MS events by the ESG system (m)			Measured coordinates of the reference point (m)			Location distance (m)
	N	E	D	N	E	D	
1	4,870,961.4	405,301.8	1251.5	4,870,960.2	405,299.5	1250.7	2.71
2	4,870,962.3	405,302.5	1249.6				3.82
3	4,870,958.6	405,303.3	1251.7				4.24

coordinates of the geometric center are listed in Table 4. The location distance is calculated to evaluate the location accuracy between the related MS events and the reference point. When the equivalent velocity of the P-wave (5545 m/s) is adopted in the single-velocity model, the average value of the location distance is 3.59 m (Table 4). The location accuracy is within an acceptable range. In addition, due to the complexity of in situ geological structures, the accuracy of the location will be affected greatly during the excavation of TBM. Therefore, the P-wave velocity in the single-velocity model should be modified frequently for MS source location based on the actual geological conditions.

3.4 Quantification of Source Parameters

The source parameters of the recorded MS signals have been calculated to estimate the evolutionary process of microseismicity by the SeisProc program in the ESG system (Cai et al. 2001). MS signals are usually caused by energy releases from rock masses. The radiated seismic energy and seismic moment are the key source parameters for quantifying the intensity of an MS signals, and can be determined from the recorded waveforms in the time domain and frequency spectra, respectively (Aki 1968; Boatwright and Fletcher 1984):

$$E = 4\pi\rho v R^2 \frac{J_c}{F_c^2}, \tag{4}$$
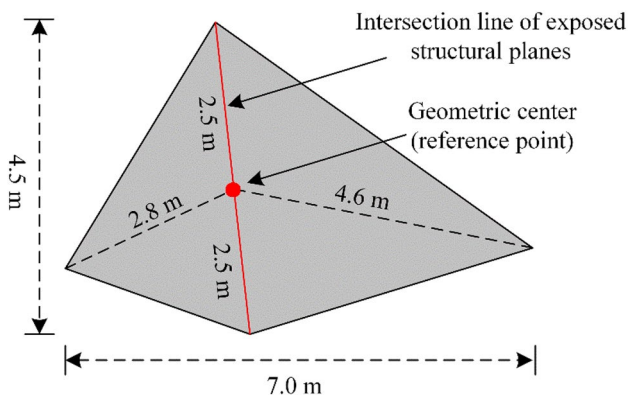
Fig. 11 Front view of this rockburst notch

$$M = 4\pi\rho v^3 R \frac{|\Omega_{oc}|}{F_c^2}, \tag{5}$$

where E and M are the seismic energy and seismic moment of the MS source, respectively; ρ is the rock mass density; v is the velocity of the body wave (P-wave or S-wave); R is the hypocentral distance from the MS source to the sensors; J_c is the energy flux, which is the integral of the square of the ground velocity from the frequency domain (Snoke et al. 1983); F_c is the average radiation coefficients for the radiation type of the seismic waves, which equals 0.52 and 0.63 for P-waves and S-waves, respectively; and Ω_{oc} represents the spectral level of the P-wave or the vector sum of the components of the S-wave (Randall 1973). In addition, when the P-wave and S-wave energy have been calculated, respectively, the total seismic energy can be estimated as shown in Eq. (6). The value of the seismic moment is taken as the average of the values obtained from the P-wave and S-wave.

$$E = E_p + E_s. \tag{6}$$

Other quantitative source parameters, namely the apparent stress, apparent volume and energy index, have been applied to evaluate the variation of the stress level and seismic inelastic deformation in rock masses (Dai et al. 2016a). The apparent stress σ_A and the apparent volume V_A are reliable estimations of the average stress release and the volume of the rock mass in the inelastic strain zone near the MS source, respectively (Wyss and Brune 1968; Mendecki 1993), which are defined as follows:

$$\sigma_A = \frac{KE}{M}, \tag{7}$$

$$V_A = \frac{M}{2\sigma_A} = \frac{M^2}{2KE}, \tag{8}$$

where σ_A and V_A represent the apparent stress and apparent volume, respectively; and K is the stiffness of the rock mass. In the risk assessment of rockbursts, the cumulative plot of the apparent volume can express the inelastic strain rate within the surrounding rock mass (Cai et al. 2001; Xiao et al. 2015). A sharp increase in the cumulative apparent volume is an indicator of the occurrence of rockbursts or large-scale fractures (Ma et al. 2016; Dai et al. 2016a).

The energy index (EI) of an MS event is defined as the ratio of the measured radiated seismic energy to the mean energy radiated by events of the same seismic moment, which represents the local stress level in the studied monitoring area (Van Aswegen and Butler 1993; Xu et al. 2015; Dai et al. 2017; Liu et al. 2019).

$$\text{EI} = \frac{E}{\bar{E}(M_0)}, \tag{9}$$

where EI is the energy index; E represents the radiated energy of an MS event; and $\bar{E}(M_0)$ represents the mean radiated energy, which is derived from the relationship between $\log E$ and $\log M$ for a given seismic moment M_0 as follows:

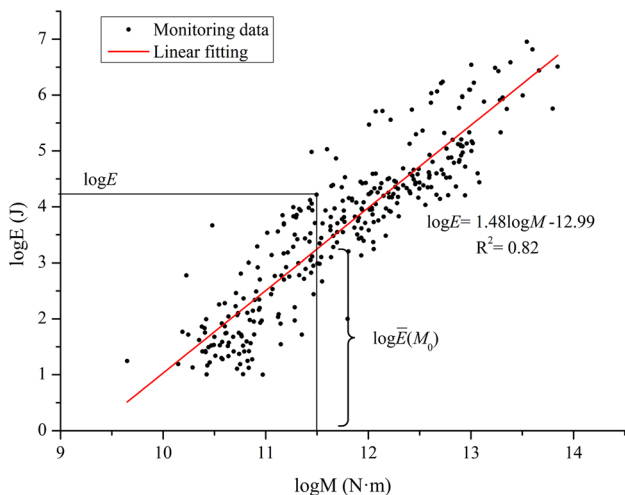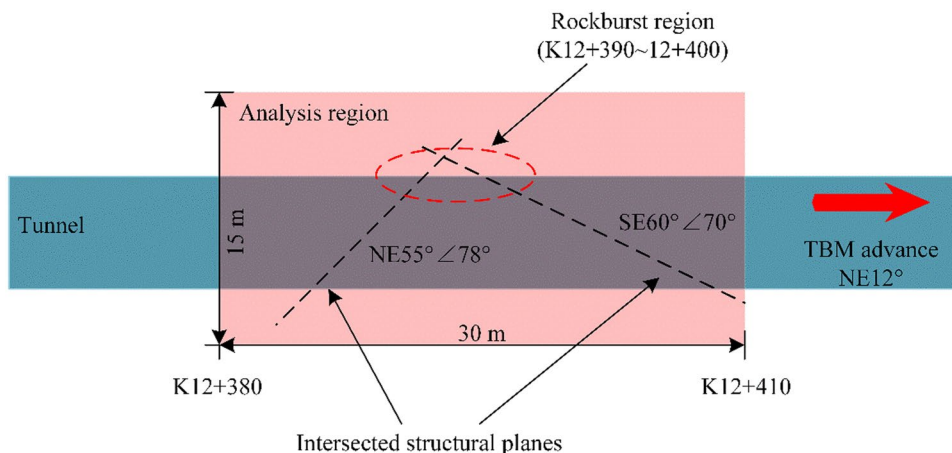$$\log \bar{E}(M_0) = d \log M_0 + c, \tag{10}$$

where d and c are constants obtained from the linear fitting of the radiated seismic energy and seismic moment. As the energy index increases, the driving stress near the seismic source becomes high. In the present study, the relationship between $\log E$ and $\log M$ is shown in Fig. 12, which is a line with an R-squared value of 0.82. Thus, the expression of the energy index can be estimated as follows by combining Eqs. (9) and (10).

$$\text{EI} = \frac{10^{12.99} E}{M_0^{1.48}}. \tag{11}$$

4 Analysis of the Microseismicity Characteristics in the 4.13 Rockburst

4.1 Selection of the Analysis Region

To reflect the whole evolutionary process of the 4.13 rockburst, the related MS events in the analysis region should be refined during the monitoring period from 10 April 2018 to 14 April 2018. According to the attitudes of two exposed structural planes in the rockburst region (Fig. 5), the range of the analysis region is selected from milestones K12+380 to K12+410 m with the area of 30×15 m (Fig. 13). The MS events in the analysis region are analyzed to present the whole evolutionary process of the rockburst subjected to TBM excavation.

4.2 Spatial Distribution of Microseismicity

Through the hypocenter location of MS events in the ESG system, a total of 113 MS events were recorded in the analysis region during the monitoring period from 0:00, 10 April to 12:00, 14 April. The vertical view of the spatial distribution of the MS event clusters in the analysis region is shown

Fig. 12 Relationship between $\log E$ and $\log M$

**Fig. 13** Vertical view of the analysis region
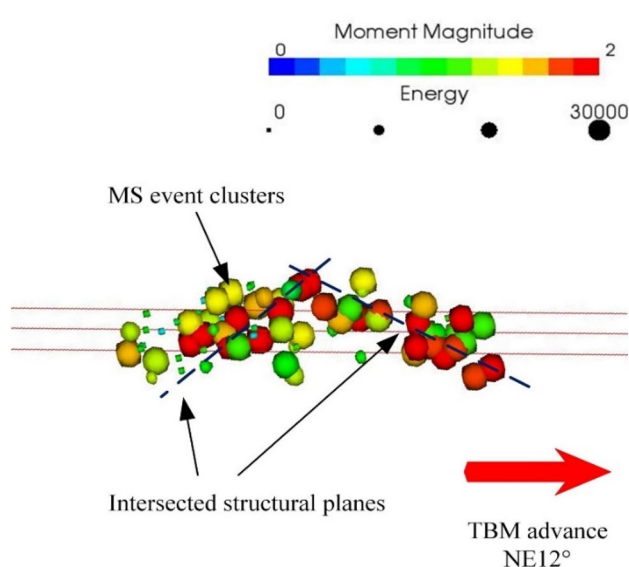
Fig. 14 Vertical view of the spatial distribution of MS event clusters in the analysis region

in Fig. 14. The colors and sizes of the spheres indicate the different moment magnitudes and radiated energies of the MS events, respectively. The large-magnitude and high-energy MS events are generally clustered around two dashed black lines in Fig. 14, whose orientations are approximately consistent with the attitudes of two exposed structural planes after the rockburst (Fig. 5).

With the further development of microseismicity, the concentration of MS event clusters represents the potentially concentrated stress area within the surrounding rock mass. The evolutionary process of the MS event density contour is presented in Fig. 15. In the analysis region, the evolutionary process of MS events can be divided into three stages, namely, the MS discrete stage, the MS concentration stage and the MS quiet stage. The features of the stages can be summarized as follows.

1. The MS discrete stage occurred from 12:00, 10 April to 12:00, 11 April. As the tunnel face moved towards the analysis region (K12 + 375–12 + 380 m), the microseis-
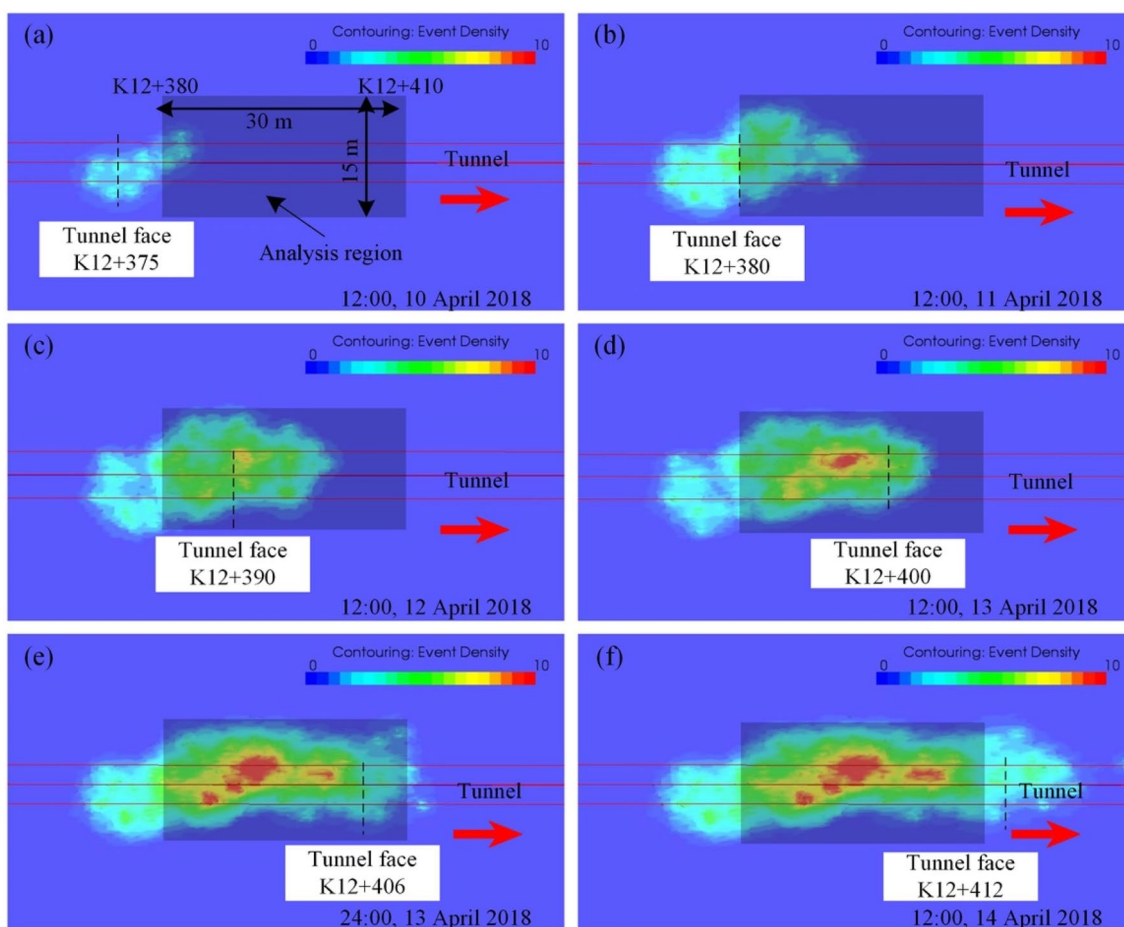
Fig. 15 Evolutionary process of the MS event density contour from **a** 12:00, 10 April to **b** 12:00, 11 April; **c** 12:00, 12 April; **d** 12:00, 13 April; **e** 24:00, 13 April; **f** 12:00, 14 April

micity gradually increased, and the distribution of MS events was discrete within the analysis region (Fig. 15a, b).

2. The MS concentration stage occurred from 12:00, 11 April to 24:00, 13 April. The microseismicity became gradually active as the tunnel face approached the rockburst region. At 12:00, 12 April, the concentration area of MS events was initially located around the left sidewall at milestone K12 + 393 m (Fig. 15c). With the progression of the tunnel face from milestones K12 + 400 to K12 + 406 m, the microseismicity became dramatically active from 12:00, 13 April to 24:00, 13 April. The concentration of MS events increased greatly at the left sidewall from milestones K12 + 390 to K12 + 400 m (Fig. 15d, e).

3. The MS quiet stage occurred from 24:00, 13 April to 12:00, 14 April. The density contour of MS events did not change further within the analysis region. The microseismicity was generally stable after the rockburst (Fig. 15f).

In the analysis region, the concentrated area of MS events is mainly located at the left sidewall of the tunnel, which coincides with actual location of the 4.13 rockburst at milestones K12 + 390–12 + 400 m. The concentration of MS events prior to the main fracture was found to be an obvious precursor of the 4.13 rockburst. The spatial distribution of MS event clusters can delineate the concentrated region of micro-fractures for recognizing potential failure zones within the rock mass. Similar precursory features have also been found in rockbursts of other types (e.g., strainbursts, fault-slip bursts and pillar bursts) (Zhang et al. 2014; Xu et al. 2016; Wang et al. 2018).
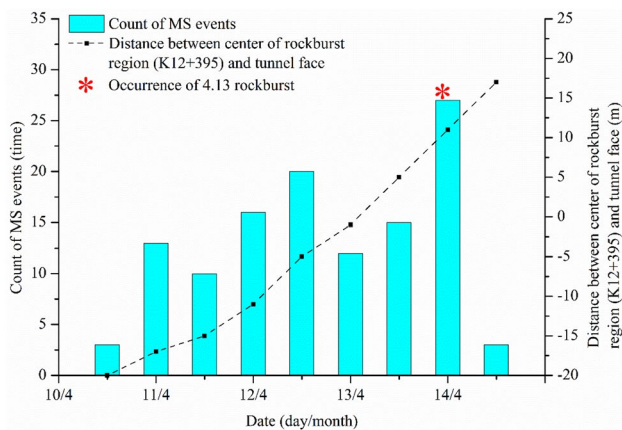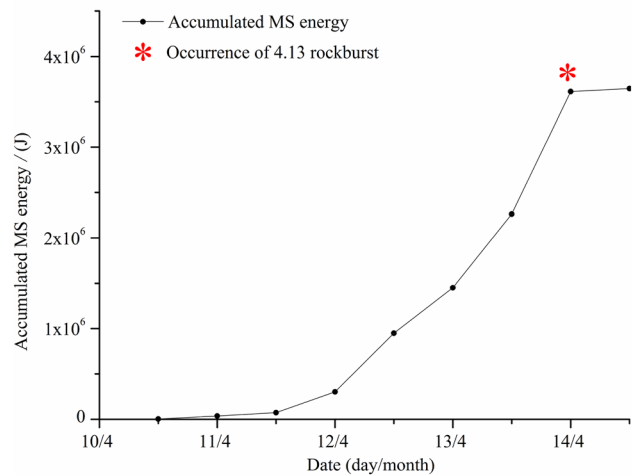

Fig. 17 Evolutionary of the accumulated MS energy

4.3 Temporal Distribution of MS Information

The temporal distribution of the MS events in the analysis region is illustrated in Fig. 16. The count of MS events was three at 12:00, 10 April, with inactive microseismicity. As the tunnel face approached the center of the rockburst region (K12 + 395 m) from 24:00, 10 April to 24:00, 12 April, the count of MS events increased gradually, and the average count of MS events was 14 per 12 h. This result may indicate aggravated damage of the rock mass with the rapid propagation of micro-fractures. When the tunnel face reached milestone K12 + 405 m, a rockburst occurred at milestones K12 + 390–12 + 400 m. The count of MS events reached a maximum value of 27 at 24:00, 13 April. After the rockburst, the count of MS events in the analysis region decreased greatly.
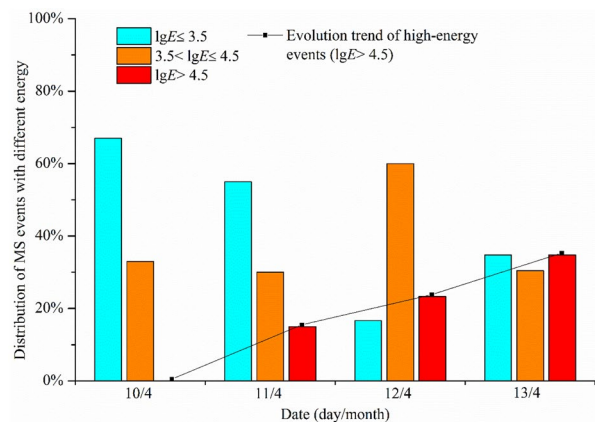

Fig. 16 Temporal distribution of the MS events associated with tunnel excavation

Fig. 18 Distribution of MS events with different energies

The evolutionary laws of the accumulated MS energy in the analysis region are shown in Figs. 17 and 18. During the monitoring period from 12:00, 10 April to 24:00, 13 April, the curve of the accumulated MS energy shows an increasing tendency (Fig. 17). Before 12 April, the MS energy release was relatively low, and an accumulated energy of 3×10^5 J was presented. From 12:00, 12 April to 24:00, 13 April, the released energy presented a gradually rapid increase, with an accumulated energy of 3.6×10^6 J. This observation may indicate that the localized stress was concentrated gradually and that high-energy events occurred frequently before the main fracture. After the 4.13 rockburst, the accumulated MS energy remained stable. Moreover, the distribution of MS events with different energies is shown in Fig. 18. Low-energy events (with logarithmic energies lesser than or equal to 3.5) were dominant on 10 April and 11 April, accounting for 67% and 55%, respectively. The proportion of high-energy MS events (with logarithmic energies greater than 4.5) gradually increased from 11 April to 13 April, which indicates a gradual increase in the aggravation of micro-fracturing near the occurrence of the 4.13 rockburst.

Therefore, by further analyzing the evolutionary laws of the MS events and the accumulated MS energy from 10 April to 14 April, it can be found that the count of MS events increased gradually, and the accumulated MS energy presented a rapid rising tendency. Moreover, the proportion of high-energy events increased steadily before the 4.13 rockburst. The abovementioned attributes can be indicators of the occurrence of this structure-type rockburst.

As mentioned in Sect. 3.4, the evolutionary laws of the accumulated apparent volume and energy index are studied to describe the seismic inelastic deformation and stress level. During the monitoring period from 12:00, 10 April to 12:00, 14 April, the laws of the logarithm energy index and accumulated apparent volume of MS events are shown in Fig. 19. From 12:00, 10 April to 12:00, 12 April, the curve of log EI presents a generally increasing trend with some fluctuations. The maximum value of log EI is 1.67. Meanwhile, the curve of the accumulated apparent volume increases in steps with small increments. In this stage, the stress level within the rock mass increased gradually, and the inelastic deformation of rock mass was relatively small. During the monitoring period from 12:00, 12 April to 12:00, 14 April, the curve of log EI decreases gradually, while the curve of the accumulated apparent volume increases progressively and presents a steep increase on 13 April. This stage indicates that the accumulated stress was gradually released and that the inelastic deformation of the rock mass was gradually accumulated. The hazard of a rockburst was aggravated in the surrounding rock mass. By analyzing the features of log EI and the accumulated apparent volume, the stress level was found to experience stages of concentration and release within the rock mass, and the inelastic deformation increased rapidly
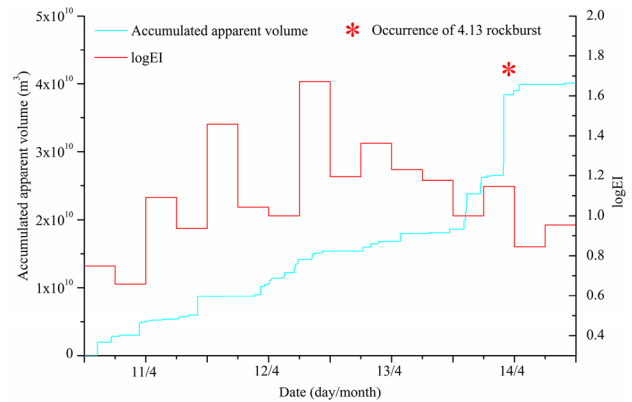
Fig. 19 Evolutionary laws of the accumulated apparent volume and energy index

before the 4.13 rockburst. Therefore, a gradual decrease in log EI with a sudden increase in the accumulated apparent volume can be precursors of this structure-type rockburst.

In rockburst cases of other types (e.g., strainbursts, fault-slip bursts and pillar bursts), the MS multi-parameter precursory characteristics were comprehensively analyzed to predict the occurrence of rockbursts (Zhang et al. 2014; Glazer 2016; Lu et al. 2018). In comparing the temporal distribution of MS characteristics of this structure-type rockburst, the distribution of MS events and the MS energy release were generally different from those of other type rockbursts, due to the presence of stiff structures. However, according to previous studies (Liu et al. 2013; Cao et al. 2016; Wang et al. 2018), the evolutionary trends of the local stress level and seismic inelastic deformation (i.e., the energy index and apparent volume) were partially similar to those of other rockbursts types, due to the stages of the local stress concentration and release during the evolutionary of rockbursts.

4.4 Fracture Mechanism in the 4.13 Rockburst

The S-wave energy and P-wave energy are two components of the seismic energy of MS events, which can be estimated by the SeisProc program in ESG systems. In seismology, the ratio of the energy of the S-wave to that of the P-wave (E_s/E_p) is an effective indicator to quantitatively identify the predominant fracture mechanism of seismic sources (Urbancic et al. 1992; Hudyma and Potvin 2010). Previous studies suggested that the energy radiated in the P-wave was a small fraction of that in the S-wave (Gibowicz et al. 1991; Xiao et al. 2016b). In general, the E_s/E_p value of 10 is regarded as a threshold to distinguish between tensile and shear failure mechanisms (Xiao et al. 2016a). MS events having low E_s/E_p values of less than 10 are usually tensile failures, while high E_s/E_p values of more than 10 indicate a shear or fault-slip mechanism. During the evolutionary process of the 4.13
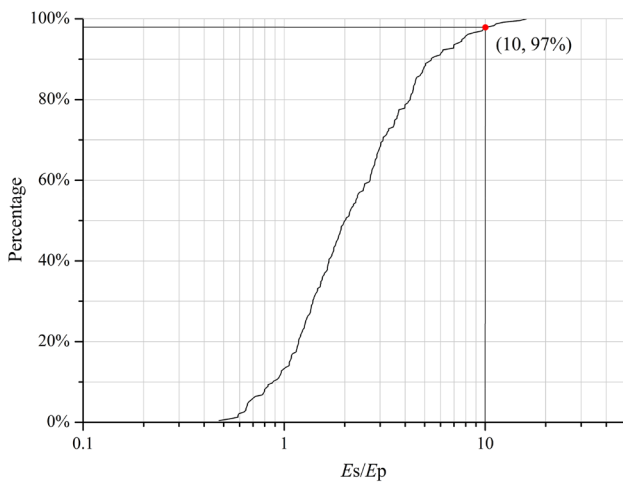
Fig. 20 Distribution of E_s/E_p values for MS events

rockburst from 10 April to 14 April, the distribution curve of E_s/E_p values is shown in Fig. 20. The E_s/E_p values of MS events range from 0.4 to 11.0, with a median value of 2. It is obvious that MS events with E_s/E_p values less than 10 account for 97%. This means that the predominant fracture mechanism was tensile during the evolutionary process of the 4.13 rockburst. According to Xiao et al. (2016b), the presence of stiff structures has an important influence on the fracture mechanism. Tensile failure dominates as the main failure type during the development of structure-type rockbursts. This conclusion is consistent with the fracture mechanism in the 4.13 rockburst. For rockbursts of other types (e.g., strainbursts and fault-slip bursts), a majority of MS monitoring results have shown that the proportion of shear failure events is much larger than that of tensile failure events (Boatwright and Fletcher 1984; Gibowicz et al. 1991; Xiao et al. 2016b).

5 Treatment Measures for Rockburst Hazards Based on MS Monitoring

A number of support measures (i.e., steel arches, steel slats and shotcrete) have been applied to minimize the hazards of mild and moderate rockbursts in the headrace tunnel. Steel arches are installed in the upper 3/4 of the cross-section circumference by using H-beam ribs, which are used to limit the deformation of the rock blocks. The spacing of the steel arches is adjusted according to the different intensities of rockbursts. Steel slats are pulled from the pockets at the rear shield of the TBM and continuously bolted to the steel arches, which can effectively constrain the movement of loose and unstable rock blocks behind the cutterhead. Steel slats can be used in the area of the crown, as well as along the tunnel sidewalls. Full-section shotcrete is normally

applied in the backup area to reinforce the surrounding rock mass (Farrokh et al. 2011). During the frequent occurrence of rockbursts from 1 April 2018 to 11 May 2018, the variations of the numbers of steel slats and steel arches are presented in Fig. 21 according to the statistics of field support measures. With the increase in microseismicity, the number of steel slats increased significantly, and the number of steel arches reached the average value of 10 per 10 meters. The support intensity should be enhanced by encrypting steel arches and steel slats within the area of active microseismicity. In short, the forms of support measures mentioned above are passive in minimizing rockburst hazards, without effectively mitigating the concentrated stress in the surrounding rock mass.

According to the results of MS monitoring, some findings about proactive treatment measures are put forward for the mitigation of rockburst hazards.

5.1 Early Warning

It is important to predict rockburst-prone zones as soon as possible. Accurate prediction ensures that special support measures can be installed as needed. Costs can be reduced by avoiding blindly installing excessive supports. According to previous researches, exhaustive investigation of geology and in situ stress fields are fundamental for the assessment of rockburst hazards (Hoek and Brown 1980; Cai 2013; Mazaira and Konicek 2015). Some comprehensive geological models and numerical indexes have been proposed to predict zones in which the rock mass may reach critical stress levels (Zhang et al. 2012b; Feng et al. 2013). However, at great depths, estimations of the stress state in rock masses are difficult based on the methods mentioned above. In the process of TBM excavation, more detailed information about the abnormal local stress within the rock mass is needed. Therefore, continuous in situ MS monitoring is an effective tool to recognize abnormally concentrated areas of MS
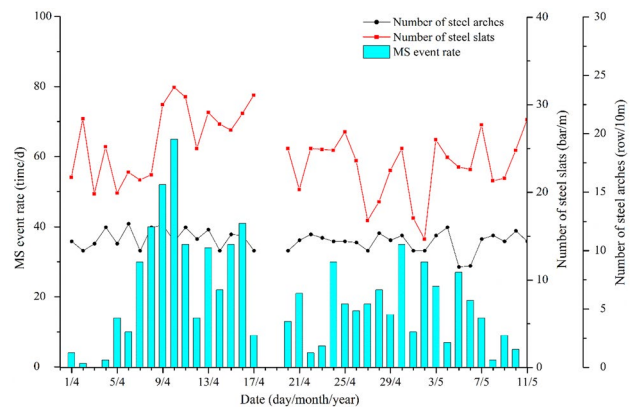

Fig. 21 Variations of the numbers of steel slats and steel arches

events, which indirectly reflects high levels of local stress concentration. In the case of the 4.13 rockburst, according to the evolutionary process of the MS event density contour in Fig. 15, the initial concentration area of MS events was located around the left sidewall at milestone K12 + 393 m on 12 April, and an abnormally concentrated area (the red region in Fig. 15d) was gradually formed around the left sidewall from milestones K12 + 390 to K12 + 400 m at 12:00, 13 April. Eventually, the rockburst occurred around the left sidewall at milestones K12 + 390–12 + 400 m at 21:55 13 April. Therefore, rockburst-prone zones can be recognized in advance through MS monitoring. Special support designs should be applied in these zones.

5.2 Rockburst Prevention Measures

Once potential rockburst-prone zones have been recognized, some prevention measures can be taken to control and reduce the rockburst hazards through three approaches: (I) optimization of the tunneling parameters, (II) preconditioning of the rock mass, (III) reinforcement and support of the rock mass. These measures should be adopted in the construction stage of TBM-excavated tunnels.

(I) Optimization of tunneling parameters. Due to the lesser flexibility of TBM excavation, it is difficult to retreat or react in response to adverse geological conditions. Some primary parameters that have great effects on the stress concentration cannot be modified easily, such as the shape and dimension of the tunnels, the excavation sequence and the excavation methods. Therefore, the optimization of the tunneling parameters of machinery is an available operation for TBM to reduce the rockburst hazards. In situ MS monitoring data are analyzed to study the relationship between microseismicity and TBM excavation. In the present study, during the monitoring period from 1 April 2018 to 11 May 2018, the excavated tunnel section (K12 + 232–12 + 675 m) had substantially similar geologic conditions (e.g., rock type, buried depth and geological features). The correlation between the MS event rate and the advance rate of the TBM is shown in Fig. 22. The MS event rate shows a gradual downward trend with decreasing TBM advance rate. The activity microseismicity is reduced by slowing the TBM advance rate. It can be inferred that the stress concentration in the surrounding rock mass is reduced sufficiently with a decrease in the unloading rate. Therefore, in tunnel sections with potential hazards of rockburst, reducing the advance rate can be suggested to mitigate the rockburst risk.

(II) Preconditioning of the rock mass. When rockburst hazards cannot be reduced by optimizing the tunneling parameters, preconditioning of the rock mass should be applied to prevent potential rockbursts by relieving the stress concentration of the rock mass prior to excavation. The widely used preconditioning methods are destress
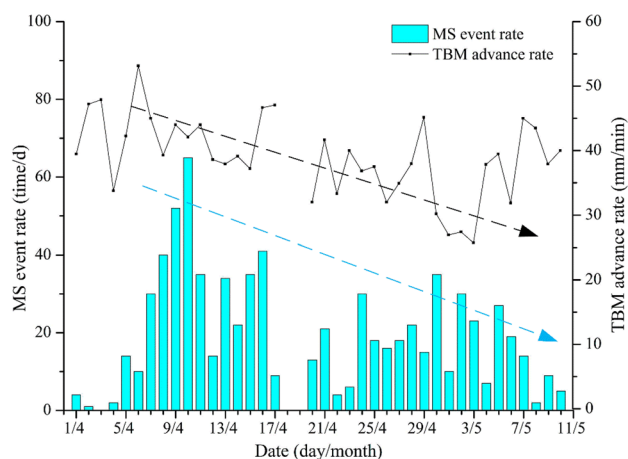

Fig. 22 Relationship between the MS event rate and the advance rate

blasting, destress drilling, hydraulic fracturing and pilot tunnels (Kaiser et al. 1996; Zhang et al. 2012b; Cai 2013). The purpose of these methods is to fracture the surrounding rock mass and migrate the high-stress concentration areas into the deeper rock mass (Kaiser et al. 1996; Konicek et al. 2013). For TBM-excavated tunnels, destress blasting cannot be carried out due to space limitations and the safety considerations of operation (Zhang et al. 2012b; Mazaira and Konicek 2015). Therefore, based on the early warning of rockburst-prone zones, destress drilling and hydraulic fracturing can be adopted to fracture localized rock masses with high stress concentrations.

(III) Support and reinforcement of the rock mass. If the rockburst risks of excavated openings are still high, support measures should be installed to protect workers and equipment, namely, by rock support and rock reinforcement. The aim of rock supports is to apply a reactive force on the opening surface to hold the fractured rock mass. The main rock supports consist of steel arches, steel slats and wire mesh, which have been applied in the headrace tunnel. The aim of rock reinforcements is to form a self-supporting rock arch around the opening and reinforce the surrounding rock mass. Engineers should take full advantage of the arching effect of the upper rock mass to maintain the stability of tunnels. The common elements of rock reinforcement are rock bolts, anchor cables and shotcretes, which are widely applied in mines and civil tunnel projects (Kaiser et al. 1996; Farrokh et al. 2011; Mazaira and Konicek 2015). For intensely and extremely intensely rockburst-prone zones, special rock supports and reinforcement systems (i.e., yielding systems) are required to provide high-energy absorption and deformation capacity, which resist the highly dynamic loads and large rock deformations (Ortlepp 2001; Cai 2013; Mazaira and Konicek 2015). In the case of the 4.13 rockburst, the highly concentrated area of MS clusters was
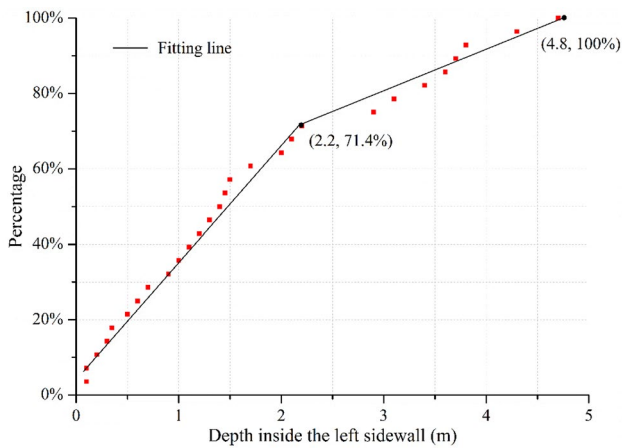
Fig. 23 Percentage of MS events developed at different depths inside the left sidewall

mainly distributed towards the interior of the left sidewall (K12 + 390–12 + 400 m) after excavation. To control the further development of the fracturing process in the localized rock mass, rock bolts should be installed passing through this region to relieve the concentrated stress and reinforce the rock mass. Figure 23 shows the percentage of MS events developed at different depths inside the left sidewall. The percentage of MS events in the depth range of [0, 2.2] (in meters) accounts for 71.4%. The maximum depth of these MS events reaches approximately 4.8 m. It can be inferred that the concentrated stress areas in the left sidewall have a depth range of approximately [0, 4.8] (in meters). Therefore, the recommended length of the rock bolts is at least 5 m. In the further construction of this headrace tunnel, some valuable references concerning the support forms (the length of the rock bolts) can be suggested to mitigate the potential rockburst hazards based on MS monitoring.

6 Conclusions

The fracture characteristics of a typical rockburst (4.13 rockburst), controlled by small-scale structural planes, were investigated in the headrace tunnel. To explore the evolutionary process of structure-type rockbursts subjected to TBM excavation, a moveable MS monitoring system was deployed to acquire real-time microseismicity characteristics during the development of the 4.13 rockburst. The conclusions can be drawn as follows.

1. The MS events in the analysis region were mainly concentrated around the left sidewall at milestone K12 + 393 m and gradually clustered 1 or 2 days prior to the 4.13 rockburst. The large-magnitude and high-energy MS events were distributed approximately along

the orientation of the two exposed structural planes. The spatial distributions of MS event clusters can delineate the concentrated areas of microseismicity to facilitate recognizing potential failure zones within rock masses.

2. Prior to the 4.13 rockburst, the count of MS events increased gradually, and the accumulated MS energy showed a rapidly rising tendency with an increasing proportion of high-energy events. The energy index showed a gradual decrease, accompanied by a sudden increase in the accumulated apparent volume. These attributes can be regarded as precursory indicators of this structure-type rockburst.

3. Based on the MS monitoring results, some proactive treatment measures are put forward for the mitigation of rockburst hazards in TBM-excavated tunnels, namely, early warning, the optimization of tunneling parameters, the preconditioning of the rock mass, and the reinforcement and support of the rock mass.

Therefore, based on MS monitoring, the preliminary achievements of this research may contribute to further understanding of the evolutionary process of rockbursts associated with small-scale structural planes. Effective guidance and valuable references can be provided for the early warning and treatment of rockbursts.

Compliance with Ethical Standards

Conflict of interest The authors declare that they have no conflict of interest.

References

Aki K (1968) Seismic displacements near a fault. J Geophys Res 73(16):5359–5376

Boatwright J, Fletcher JB (1984) The partition of radiated energy between P and S waves. B Seismol Soc Am 74(2):361–376

Cai M (2013) Principles of rock support in burst-prone ground. Tunn Undergr Sp Technol 36:46–56

Cai M, Kaiser PK, Martin CD (2001) Quantification of rock mass damage in underground excavations from microseismic event monitoring. Int J Rock Mech Min Sci 38(8):1135–1145

Cao AY, Dou LM, Wang CB, Yao XX, Dong JY, Gu Y (2016) Microseismic precursory characteristics of rock burst hazard in mining areas near a large residual coal pillar: a case study from Xuzhuang coal mine, Xuzhou, China. Rock Mech Rock Eng 49:4407–4422

Chen BR, Feng XT, Li QP, Luo RZ, Li SJ (2015) Rock burst intensity classification based on the radiated energy with damage intensity at Jinping II hydropower station, China. Rock Mech Rock Eng 48(1):289–303

Cheng F, Liu JP, Qu NN, Mao M, Zhou LM (2014) Two-dimensional pre-stack reverse time imaging based on tunnel space. J Appl Geophys 104:106–113

Cook NGW (1965) The failure of rock. Int J Rock Mech Min Sci Geomech Abstr 2(4):389–403

Dai F, Li B, Xu NW, Fan YL, Zhang CQ (2016a) Deformation forecasting and stability analysis of large-scale underground powerhouse caverns from microseismic monitoring. Int J Rock Mech Min Sci 86:269–281

Dai F, Li B, Xu NW, Meng GT, Wu JY, Fan YL (2016b) Microseismic monitoring of the left bank slope at the Baihetan hydropower station, China. Rock Mech Rock Eng 50(1):225–232

Dai F, Li B, Xu NW, Zhu YG (2017) Microseismic early warning of surrounding rock mass deformation in the underground power-house of the Houziyan hydropower station, China. Tunn Undergr Sp Tech 62:64–74

Farrokh E, Rostami J, Laughton C (2011) Analysis of unit supporting time and support installation time for open TBMs. Rock Mech Rock Eng 44(4):431–445

Feng XT, Chen BR, Li SJ, Zhang CQ, Xiao YX, Feng GL, Zhou H, Qiu SL, Zhao ZN, Yu Y, Chen DF, Ming HJ (2012) Studies on the evolution process of rockbursts in deep tunnels. J Rock Mech Geotech Eng 4(4):289–295

Feng XT, Chen BR, Zhang CQ, Li SJ, Wu SY (2013) Mechanism, warning and dynamic control of rockburst development processes. Science Press, Beijing **(in Chinese)**

Gibowicz SJ, Young RP, Talebi S, Rawlence DJ (1991) Source parameters of seismic events at the underground research laboratory in Manitoba, Canada: scaling relations for events with moment magnitude smaller than -2. B Seismol Soc Am 81(4):1157–1182

Glazer SN (2016) Mine seismology: data analysis and interpretation. Springer International Publishing, Switzerland

Hoek E, Brown ET (1980) Underground excavations in rock. The Institute of Mining and Metallurgy, London

Hudyma M, Potvin YH (2010) An engineering approach to seismic risk management in hardrock mines. Rock Mech Rock Eng 43(6):891–906

Kaiser PK, Tannant DD, McCreath DR (1996) Canadian rockburst support handbook. Geomechanics Research Centre/Laurentian University, Sudbury/Ontario

Konicek P, Soucek K, Stas L, Singh R (2013) Long-hole destress blasting for rockburst control during deep underground coal mining. Int J Rock Mech Min Sci 61:141–153

Krietsch H, Gischig V, Evans K, Doetsch J, Dutler NO, Valley B, Amann F (2018) Stress measurements for an in situ stimulation experiment in crystalline rock: integration of induced seismicity, stress relief and hydraulic methods. Rock Mech Rock Eng 20:1–26

Leśniak A, Isakow Z (2009) Space–time clustering of seismic events and hazard assessment in the Zabrze-Bielszowice coal mine, Poland. Int J Rock Mech Min Sci 46(5):918–928

Li SC, Liu B, Xu XJ, Nie LC, Liu ZY, Song J, Sun HF, Chen L, Fan KR (2017a) An overview of ahead geological prospecting in tunneling. Tunn Undergr Sp Technol 63:69–94

Li HB, Liu MC, Xing WB, Shao S, Zhou JW (2017b) Failure mechanisms and evolution assessment of the excavation damaged zones in a large-scale and deeply buried underground powerhouse. Rock Mech Rock Eng 50(7):1883–1900

Liu JP, Feng XT, Li YH, Xu SD, Sheng Y (2013) Studies on temporal and spatial variation of microseismic activities in a deep metal mine. Int J Rock Mech Min Sci 60:171–179

Liu GF, Feng XT, Feng GL, Chen BR, Chen DF, Duan SQ (2016) A method for dynamic risk assessment and management of rockbursts in drill and blast tunnels. Rock Mech Rock Eng 49(8):3257–3279

Liu QS, Liu JP, Pan YC, Zhang XP, Peng XX, Gong QM, Du LJ (2017) A wear rule and cutter life prediction model of a 20-in TBM cutter for granite: a case study of a water conveyance tunnel in China. Rock Mech Rock Eng 50(5):1303–1320

Liu F, Ma TH, Tang CA, Chen F (2018) Prediction of rockburst in tunnels at the Jinping II hydropower station using microseismic monitoring technique. Tunn Undergr Sp Technol 81:480–493

Liu F, Tang CA, Ma TH, Tang LX (2019) Characterizing rockbursts along a structural plane in a tunnel of the Hanjiang-to-Weihe river diversion project by microseismic monitoring. Rock Mech Rock Eng 52:1835–1856

Lu CP, Liu Y, Zhang N, Zhao TB, Wang HY (2018) In-situ and experimental investigations of rockburst precursor and prevention induced by fault slip. Int J Rock Mech Min Sci 108:86–95

Ma TH, Tang CA, Tang LX, Zhuang DY, Wang L (2015) Rockburst characteristics and microseismic monitoring of deep-buried tunnels for Jinping II hydropower station. Tunn Undergr Sp Technol 49:345–368

Ma K, Tang CA, Wang LX, Tang DH, Zhuang DY, Zhang QB, Zhao J (2016) Stability analysis of underground oil storage caverns by an integrated numerical and microseismic monitoring approach. Tunn Undergr Sp Technol 54:81–91

Ma CS, Chen WZ, Tan XJ, Tian HM, Yang JP, Yu JX (2018) Novel rockburst criterion based on the TBM tunnel construction of the Neelum–Jhelum (NJ) hydroelectric project in Pakistan. Tunn Undergr Sp Technol 81:391–402

Mallet S (1999) A wavelet tour of signal processing, 2nd edn. Academic Press, Waltham

Mazaira A, Konicek P (2015) Intense rockburst impacts in deep underground construction and their prevention. Can Geotech J 52(10):1426–1439

Mcgarr A, Bicknell J, Sembera E, Green RWE (1989) Analysis of exceptionally large tremors in two gold mining districts of South Africa. Pure Appl Geophys 129(3–4):295–307

Mendecki AJ (1993) Keynote address: real time quantitative seismology in mines. In: Proceedings of third international symposium on rock-bursts and seismicity in mines 16–18 August 1993. Kingston, Ontario, Canada, pp 287–295

Mendecki AJ (1997) Seismic monitoring in mines. Chapman & Hall, London

Michael RS, Thomas J (2018) Fault induced rock bursts and microtremors: experiences from the Gotthard base tunnel. Tunn Undergr Sp Technol 81:358–366

Naji AM, Emad MZ, Rehman H, Yoo H (2019) Geological and geomechanical heterogeneity in deep hydropower tunnels: a rock burst failure case study. Tunn Undergr Sp Technol 84:507–521

Ortlepp WD (2000) Observation of mining-induced faults in an intact rock mass at depth. Int J Rock Mech Min Sci 37(1):423–436

Ortlepp WD (2001) The behaviour of tunnels at great depth under large static and dynamic pressures. Tunn Undergr Sp Technol 16(1):41–48

Otto R, Button E, Bretterebner H, Schwab P (2002) The application of TRT-true reflection tomography-at the Unterwald tunnel. Felsbau 20(2):51–56

Randall MJ (1973) The spectral theory of seismic sources. B Seismol Soc Am 63(3):1133–1144

Sjöberg J, Christiansson R, Hudson JA (2003) ISRM suggested methods for rock stress estimation—Part 2: overcoring methods. Int J Rock Mech Min Sci 40(7–8):999–1010

Snelling PE, Godin L, McKinnon SD (2013) The role of geologic structure and stress in triggering remote seismicity in Creighton mine, Sudbury, Canada. Int J Rock Mech Min Sci 58:166–179

Snoke J, Linde A, Sacks I (1983) Apparent stress: an estimate of the stress drop. B Seismol Soc Am 73(2):339–348

Tang CA, Wang J, Zhang J (2010) Preliminary engineering application of microseismic monitoring technique to rockburst prediction in tunneling of Jinping II project. J Rock Mech Geotech Eng 2(3):193–208

The National Standards Compilation Group of People's Republic of China (2008) Code for engineering geological investigation of

water resources and hydropower (GB50487-2008). China Planning Press, Beijing **(in Chinese)**

Trifu CI, Shumila V (2010) Microseismic monitoring of a controlled collapse in field II at Ocnele Mari, Romania. Pure Appl Geophys 167(1–2):27–42

Urbancic TI, Trifu CI (2000) Recent advances in seismic monitoring technology at Canadian mines. J Appl Geophys 45(4):225–237

Urbancic TI, Young RP, Bird S, Bawden W (1992) Microseismic source parameters and their use in characterizing rock mass behaviour: considerations from Strathcona mine. In: Proceedings of 94th annual general meeting of the CIM: rock mechanics and strata control sessions, Montreal, 26–30 April 1992, pp 36–47

Van Aswegen G, Butler AG (1993) Applications of quantitative seismology in South Africa gold mines. In: Proceedings of third international symposium on rockbursts and seismicity in mines, 16–18 August 1993. Kingston, Ontario, Canada, pp 261–266

Wang GF, Gong SY, Dou LM, Wang H, Cai W, Cao AY (2018) Rockburst characteristics in syncline regions and microseismic precursors based on energy density clouds. Tunn Undergr Sp Technol 81:83–93

Wohnlich M (1999) In-situ stress measurements (post-excavation) in the boreholes GMT 98-001/GMT 98-003 and GMT 99-006. NAGRA, Wettingen

Wyss M, Brune JN (1968) Seismic moment, stress, and source dimensions for earthquakes in the California-Nevada region. J Geophys Res 73(14):4681–4694

Xiao YX, Feng XT, Hudson JA, Chen BR, Feng GL, Liu JP (2015) ISRM suggested method for in situ microseismic monitoring of the fracturing process in rock masses. Rock Mech Rock Eng 49(1):343–369

Xiao YX, Feng XT, Feng GL, Liu HJ, Jiang Q, Qiu SL (2016a) Mechanism of evolution of stress–structure controlled collapse of surrounding rock in caverns: a case study from the Baihetan hydropower station in China. Tunn Undergr Sp Technol 51:56–67

Xiao YX, Feng XT, Li SJ, Feng GL, Yu Y (2016b) Rock mass failure mechanisms during the evolution process of rockbursts in tunnels. Int J Rock Mech Min Sci 83:174–181

Xu NW, Tang CA, Li LC, Zhou Z, Sha C, Liang ZZ, Yang JY (2011) Microseismic monitoring and stability analysis of the left bank slope in Jinping first stage hydropower station in southwestern China. Int J Rock Mech Min Sci 48(6):950–963

Xu NW, Li TB, Dai F, Li B, Zhu YG, Yang DS (2015) Microseismic monitoring and stability evaluation for the large scale under- ground caverns at the Houziyan hydropower station in Southwest China. Eng Geol 188:48–67

Xu NW, Li TB, Dai F, Zhang R, Tang CA, Tang LX (2016) Microseismic monitoring of strainburst activities in deep tunnels at the Jinping II hydropower station, China. Rock Mech Rock Eng 49(3):981–1000

Yamamoto T, Shirasagi S, Yokota Y, Koizumi Y (2011) Imaging geological conditions ahead of a tunnel face using three-dimensional seismic reflector tracing system. Int J JCRM 6(1):23–31

Young RP, Collins DS, Reyes-Montes JM, Baker C (2004) Quantification and interpretation of seismicity. Int J Rock Mech Min Sci 41(8):1317–1327

Zhang XP, Zhang Q (2017) Distinction of crack nature in brittle rock-like materials: a numerical study based on moment tensors. Rock Mech Rock Eng 50(10):2837–2845

Zhang CQ, Feng XT, Zhou H, Qiu SL, Wu WP (2012a) Case histories of four extremely intense rockbursts in deep tunnels. Rock Mech Rock Eng 45(3):275–288

Zhang CQ, Feng XT, Zhou H, Qiu SL, Wu WP (2012b) A top pilot tunnel preconditioning method for the prevention of extremely intense rockbursts in deep tunnels excavated by TBMs. Rock Mech Rock Eng 45(3):289–309

Zhang PH, Yang TH, Yu QL, Xu T, Zhu WC, Liu HG, Zhou JR, Zhao YC (2014) Microseismicity induced by fault activation during the fracture process of a crown pillar. Rock Mech Rock Eng 48(4):1673–1682

Zhang XP, Zhang Q, Wu SC (2017) Acoustic emission characteristics of the rock-like material containing a single flaw under different compressive loading rates. Comput Geotech 83:83–97

Zhao TB, Guo WY, Tan YL, Lu CP, Wang CW (2017) Case histories of rock bursts under complicated geological conditions. Bull Eng Geol Environ 77(4):1529–1545

Zhou H, Meng FZ, Zhang CQ, Hu DW, Yang FJ, Lu JJ (2014) Analysis of rockburst mechanisms induced by structural planes in deep tunnels. Bull Eng Geol Environ 74(4):1435–1451